Autonomous Wind Tunnel Free-Flight of a Flapping Wing MAV

C. De Wagter & A. Koopmans & G. de Croon & B. Remes & R. Ruijsink*

April 30, 2013

Abstract

A low-cost high performance control system is developed to enable autonomous untethered flight inside a wind tunnel. Such autonomous flight is desirable for aerodynamic experiments on flapping wing MAVs, since fixing the fuselage has been shown to significantly alter wing deformations, air flow and performance on vehicles with a periodically moving fuselage. To obtain autonomous untethered flight, 3D position information is obtained from off-board WiiMote infrared tracking sensors with a total system accuracy of 0.8mm and an update rate of 80Hz in a quarter cubical meter control box. This information is sent to a 1.5 gram onboard autopilot containing communication, inertial measurements as well as onboard infrared tracking of an in-tunnel LED to achieve the high performance control needed to position itself precisely in the wind tunnel flow. Flight tests were performed with the 16 gram flapping wing MAV DelFly II. The achieved control performance is shown to be sufficient for many new research purposes, like researching the influence of a fixed fuselage in flapping wing aerodynamic measurements and obtaining more precise performance characteristics.

1   Introduction

The aerodynamics of flapping wings is a broadly studied subject. Besides theoretical, numerical, and animal studies [19, 2, 13, 20, 5, 3, 11, 21], there is an increasing number of studies on artificial wings of flapping wing Micro Air Vehicles (MAVs) (e.g., [4, 7, 12, 17]). Fluid-structure interaction makes the study of flapping wing aerodynamics computationally very complex, but also makes it hard to obtain measurements without any external influences.

Until now, studies on flapping wing MAVs are always performed with a fixed fuselage [6, 8, 9, 7, 12, 10, 17]. For example, research on the *DelFly II* flapping wing MAV (Fig. 1) has always been studied with a fixed fuselage be it for computational fluid dynamics, force measurements[6], or Particle Image Velocimetry

*Micro Aerial Vehicle Lab, Faculty of Aerospace Engineering, Delft University of Technology, Kluyverweg 1, 2629HS Delft, the Netherlands, Contact: c.dewagter@tudelft.nl

(PIV)[9, 10]. While DelFly II was designed to minimize the fuselage rocking motion, some inevitable motion remains. This means that a fixed support changes the flight conditions of the otherwise periodically moving fuselage.

This paper proposes a low cost high performance system that enables the DelFly II to fly untethered at a fixed location in a constant wind flow. This allows for new highly needed insight [15, 18] to be obtained about the aerodynamics, free flight deformations, flight characteristics, performance aspects and transient behavior of flapping wing MAVs. It is a first step toward free-flight PIV measurements in a wind tunnel[16]. While this has been achieved with living creatures [5, 3, 11], it has not been done before with a flapping wing MAV.

In the remainder of the paper, first the system setup is explained (Section 2). Subsequently, in Section 3, the sensor fusion necessary to estimate the DelFly's state is discussed. The manner in which the state estimate is used for controlling the DelFly during free flight is explained in Section 4. Then, results are discussed of stationary (Section 5) and transient (Section 6) tests in the wind tunnel. Finally, conclusions are drawn in Section 7.

Figure 1: DelFly II has a double pair of flapping wings, driven by a 2 Watt sensorless brushless motor that drives gears with pushrods to the wings. The horizontal stabilizer has an elevator and the vertical stabilizer a rudder. Both are driven by servo's. The flapping frequency is controlled by the power setting of the main motor controller. Onboard electronics comprise of a radio or modem for communication, an autopilot processor with sensors and a special made brushless motor controller.

2   System Overview

Precise high performance position control is an important requirement to allow close up measurements, while the characteristics of the vehicle should not be altered by adding too much weight. Therefore a combined onboard plus off-board solution is used.

A high update rate tracking system measures the position of the DelFly externally. Simultaneously, an onboard microcontroller performs inertial measurements. It also reads analysis results of the onboard camera looking at an infrared LED placed in the tunnel in front of the DelFly and which acts as a heading reference [1]. External position measurements are sent to the DelFly to allow full onboard fast control loops to follow the desired setpoints as illustrated in Fig. 2).
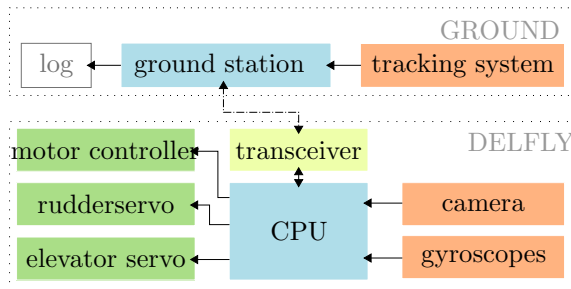

Figure 2: Schematic overview of all the system components. It consists of a ground section with the heavier sensors and a section onboard the DelFly with the high rate low latency sensors to allow light high performance control.

Position data is gathered and processed on the ground and packed with commands. These are then sent to the DelFly autopilot over the wireless Bluetooth link. Final data merging and control is done onboard while telemetry is being returned to the ground for logging purposes (Fig. 3).
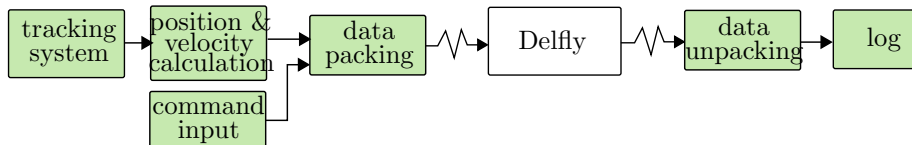

Figure 3: Flow diagram of ground station functionality.

2.1 Onboard: Autopilot System

A 20 Mega-Instructions Per Second (MIPS) capable 4 by 4 millimeter microcontroller[1] is heart of the autopilot system. A Bluetooth serial modem[2] is used as bidirectional digital communication link at 38400bps. A Wii-Mote camera sensor is stripped down to 0.33 gram at 8 by 8 by 4 millimeter and placed onboard looking forward. It provides 200Hz pixel positions of up to 4 LED. Finally the Invensense ITG3200 MEMS 3-axis gyro provides up to 1kHz of inertial measurements. An overview picture is found in Fig. 4.
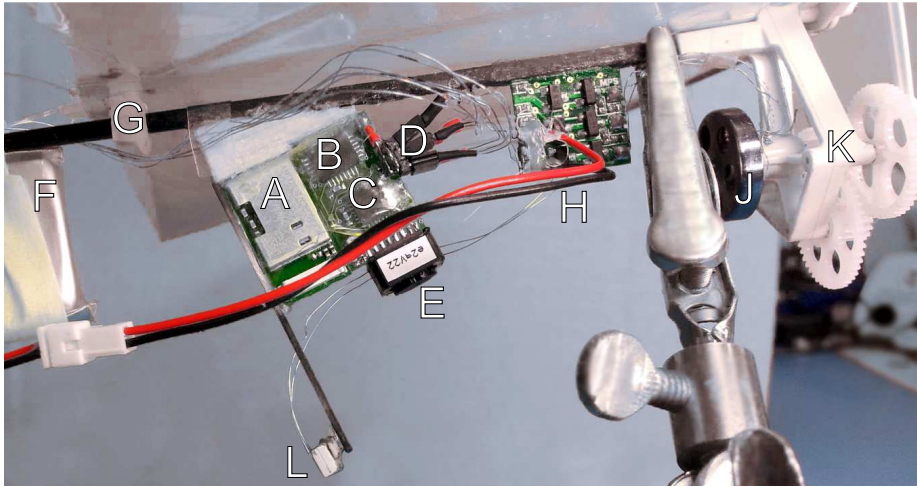
---

[1] AVR ATmega88PA
[2] Panasonic PAN1321

Figure 4: Side view of the DelFly. **(A)** Bluetooth module, **(B)** 3-axis gyroscope, **(C)** CPU, **(D)** Servo and motor connectors (from top to bottom: motor controller, elevator servo, rudder servo), **(E)** WiiMote Camera, **(F)** 180mAh LiPo battery, **(G)** Trailing edge tensioner, **(H)** Motor controller, **(J)** Brushless motor, **(K)** Gear housing, **(L)** Tracking LED

The WiiMote camera is chosen because it is cheap, available, fast, small, and all the preprocessing is already done by the build-in integrated circuit (IC) in the camera. Calibration tests using stepper-motor tables with a moving LED showed that no camera distortion worth un-distorting was present. Furthermore it interprets the image, finds the four brightest Infrared (IR) point, and calculates the respective x and y coordinates, which takes a significant workload away from the autopilot microcontroller. The WiiMote camera has a pixel resolution of 128 by 96 of sufficient quality to allow interpolation up to 1024 by 768 subpixels. This corresponds to 0.03° with the 44 by 33 degree field of view.

2.2 Off board Tracking System

The tracking system consists of two non-modified WiiMote controllers mounted on a rigid support. Using multiple view camera geometry the observed LED position is reconstructed in 3D.

3 Sensor Fusion

3.1 Linear LS Triangulation

After un-distortion of lens effects, a camera can be well represented by the pinhole model [14] which maps point $\vec{x}$ in homogeneous world coordinates into its projection $\vec{u}$.
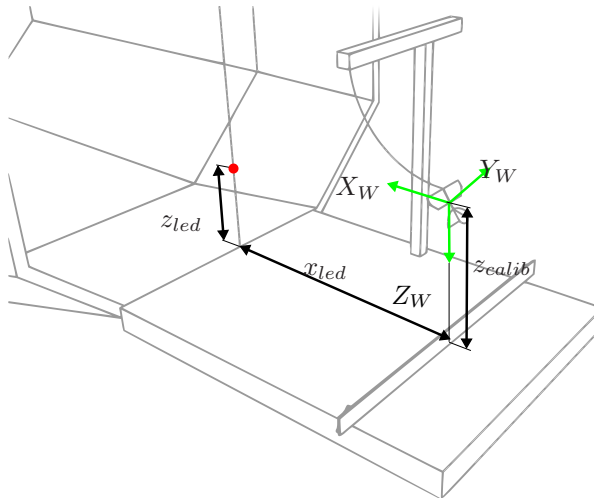
Figure 5: Schematic view of the OJF (Open Jet Facility) wind tunnel. The octagonal wind tunnel nozzle is on the left, with a LED (red) attached to a fish wire stretched over the opening. The DelFly II is attached to the T-shaped beam by means of a thin wire. The tracking cameras are mounted on the horizontal beam across the platform, and look towards the DelFly at a 45° angle.

$$s\vec{u} = N[R|t]\vec{x}$$

The camera observation $\vec{u}$ of an observed LED at position $\vec{x}$ is defined by $\vec{u} = P\vec{x}$, with $\vec{x} = (x, y, z, w)$ the position vector and P is the camera matrix. Vector $\vec{u}$ is in homogeneous coordinates, i.e. $\vec{u} = s(u, v, 1)^\top$, where u and v are the observed point coordinates, and s is an unknown scale factor. Denoting $p_i^\top$ as the ith row of matrix P, we can rewrite $\mathbf{u} = P\mathbf{x}$ as

$$su = \vec{p_1}^\top \vec{x}, \quad sv = \vec{p_2}^\top \vec{x}, \quad s = \vec{p_3}^\top \vec{x} \tag{1}$$

Eliminating s using the last equation, we have

$$u\vec{p_3}^\top \vec{x} = \vec{p_1}^\top \vec{x} \tag{2}$$
$$v\vec{p_3}^\top \vec{x} = \vec{p_2}^\top \vec{x} \tag{3}$$

From the two views we have 4 linear equations in the coordinates of $\vec{x}$, written in the form $A\vec{x} = \vec{0}$ with A a 4×4 matrix. For non-infinity target $\vec{x} = (x, y, z, 1)^\top$ is set to reduce homogeneous equations to a set of four non-homogeneous equations with three unknowns. To combine the measurements, the observed point $\vec{x}$ is also expressed in the reference frame of the second camera. This is done introducing rotation matrix R and translation vector t which describe the known relative position and orientation of the two cameras. We also rewrite R and t in homogeneous coordinate format. The camera matrixes for cameras 1 and 2 are

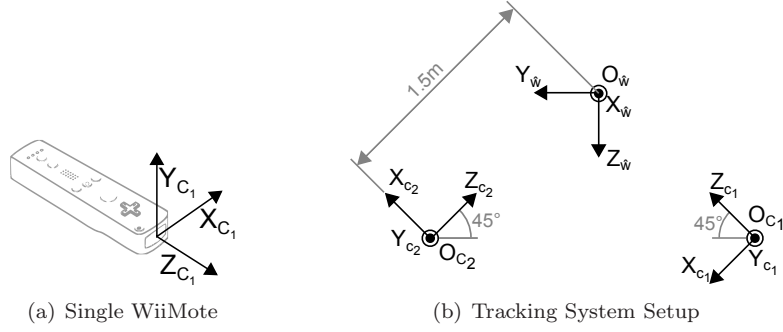(a) Single WiiMote (b) Tracking System Setup

Figure 6: Axis definition of a Wiimote and Tracking System with two WiiMotes. The realive positioning is shown in subfigure (b)

$$P_1 = N_1[\vec{I}_3 \ \vec{0}] \tag{4}$$
$$P_2 = N_2[R \ T] \tag{5}$$

Now using Eq. 3 and considering both measurements with the camera matrices P_1 and P_2, we can construct matrix A as

$$A = \begin{bmatrix} u_1 \vec{p}_1^\top(3) - \vec{p}_1^\top(1) \\ v_1 \vec{p}_1^\top(3) - \vec{p}_1^\top(2) \\ u_2 \vec{p}_2^\top(3) - \vec{p}_2^\top(1) \\ v_2 \vec{p}_2^\top(3) - \vec{p}_2^\top(2) \end{bmatrix} \vec{x}$$

where the number in brackets indicates the row vector taken from the respective matrix. The fourth element of $\mathbf{x}$ is 1 and brought to the right because of the assumption of the homogeneous coordinate being finite. Writing A as $[\vec{a}_1 \ \vec{a}_2 \ \vec{a}_3 \ \vec{a}_4]$ with each vector $\vec{a}_n$ representing a column, we get

$$\begin{bmatrix} \vec{a}_1 \ \vec{a}_2 \ \vec{a}_3 \end{bmatrix} (x, y, z)^\top = -\vec{a}_4$$

This non-homogeneous equation can be solved by using the left pseudo inverse

$$\vec{x} = -(A^\top A)^{-1} A^\top \vec{a}_4$$

which gives $\vec{x}_{C_1}$ relative to camera 1, as depicted by the subscript C_1. To express $\vec{u}$ in the windtunnel coordinates $\mathcal{F}_{\hat{w}}$ (see Fig. 6) an extra transformation is applied

$$\vec{x}_{\hat{w}} = R_{C_1}^{\hat{w}}(\vec{x}_{C_1} + \vec{T}_{C_1}^{\hat{w}}) \tag{6}$$

6

where $\vec{x}_{\hat{w}}$ is the coordinate in $\mathcal{F}_{\hat{w}}$, $R_{C_1}^{\hat{w}}$ the rotation matrix describing the rotation from $\mathcal{F}_{C_1}$ to $\mathcal{F}_{\hat{w}}$, and where $\vec{T}_{C_1}^{\hat{w}}$ describes the position of the origin $\mathcal{O}_{\hat{w}}$ relative to the origin of $\mathcal{O}_{C_1}$, expressed in $\mathcal{F}_{C_1}$. Finally the rotation and translation of the dual camera setup (Fig. 6) are

$$\vec{T}_{C_1}^{\hat{w}} = \begin{bmatrix} 0 \\ 0 \\ 1.5 \end{bmatrix} \qquad R_{C_1}^{\hat{w}} = \begin{bmatrix} 0 & 1 & 0 \\ \cos 45° & 0 & \cos 45° \\ \cos 45° & 0 & -\cos 45° \end{bmatrix} \qquad (7)$$

3.2 Velocity

The velocity is obtained by taking the discrete derivative directly from the position measurements.

$$v_k = \frac{x_k - x_{k-1}}{\Delta_T}$$

where v_k is the velocity at time step k, x_k the position at time k and Δ_T the time step size. This is done by a discrete Kalman filter to smoothen the results and fill the gaps when the LED was not detected during a frame.

3.3 Heading

To significantly improve the observability of the DelFly attitude, during slow hovering flight of DelFly with high pitch angle a heading reference is computed from an on-board camera combined with an IR Light Emitting Diode (LED) placed in the middle of the wind tunnel. The horizontal pixel coordinate $\vec{u}$ as seen in DelFly camera frame $\mathcal{F}_C$ (Fig. 7) of the reference LED is transformed to the heading χ in degrees by

$$\chi = s_u(u - c_u) \qquad (8)$$

where s_u is the angle one horizontal pixel represents and c_u the center pixel that defines the mid point of the field of view in pixels.

At faster forward flight the DelFly flies at much smaller pitch angles and the on-board camera is no longer looking forward and is therefore unable to see the reference LED inside the wind tunnel. The heading χ is therefore calculated from difference in horizontal positions of 2 LED on the ground about a meter in front of the DelFly

$$\chi = \tan^{-1}\left(\frac{u_1 - u_2}{v_1 - v_2}\right) \qquad (9)$$

where u is the horizontal pixel coordinate and v the vertical pixel coordinate of their respective pixel. Small-angle approximation is applied to save on calculation time on the on-board processor.
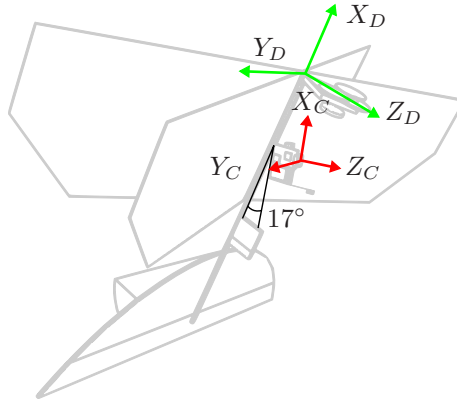
7

Figure 7: Axis definition of the Delfly body reference frame $\mathcal{F}_D$ and the on-board camera reference frame $\mathcal{F}_C$. The autopilot PCB is rotated 17 degrees around the Y_D axis. The on-board camera reference frame is defined with the X-axis pointing upward, the Y-axis pointing to the negative Y_D axis, and Z-axis pointing in the flight direction and indicated with a C subscript.

3.4 Calibration and Accuracy

At first the *extrinsic* parameters needed for the Linear-LS triangulation method of the stereoscopic camera pair is determined using OpenCV's *stereoCalibration2* routine. Then the *inertial* calibration, which maps the observations from the stereo camera frame $\mathcal{F}_w$ to the actual wind tunnel flight frame $\mathcal{F}_{\hat{w}}$. A rectangular LED board was placed with one corner at the point that should become the origin of the new coordinate system and its two side nicely aligned with the tunnel. A reading with the tracking system was taken and the TRIAD algorithm was used to acquire the correction rotation matrix and translation vector.

The accuracy of the hardware and algorithm was checked by moving the LED in a predetermined pattern by means of a micrometer precise stepper motor table. The setup was tested with a dog-leg pattern. The LED was moved 300 mm from the left to the right, and then 200 mm backwards (positive z direction). (Fig. 8)

The standard deviation of the error is 0.3734 mm in the x-direction and 0.6378 mm in the z-direction. It can be seen that the error shows a saw-tooth behavior probably caused by the pixel rounding of the cameras. Nevertheless the average deviation is sub millimeter and maximum error never more than 2 millimeters.
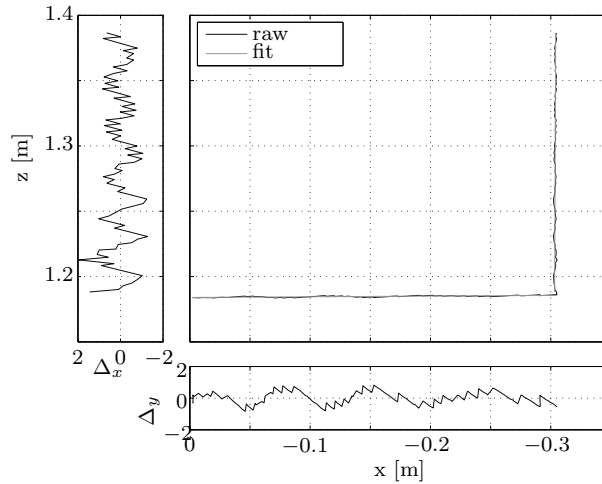
Figure 8: Calibration track with corresponding errors. Coordinates are expressed in the camera reference frame $\mathcal{F}_{C_1}$.
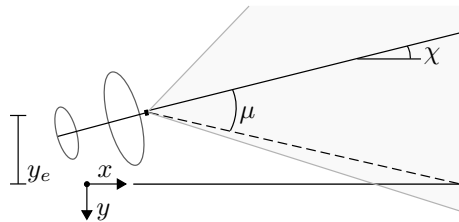

Figure 9: Schematic top-view of an lateral error. The red dot indicates the location of the infra red reference LED. μ is the angle towards the LED while χ is the heading of DelFly II

4 Controller Architecture

For the controller design, an important factor is the limited processing power available. Therefore the design goals focus on getting the required performance with sufficiently low processing power.

4.1 Lateral Control of Slow Forward Flight

As the distance of the DelFly to its heading LED is constant, the angle μ at which DelFly sees the target is homogenous. A heading controller is set to minimize μ. This constant steering towards the LED $K_\mu\mu$ creates a P-controller minimizing the lateral offset (Fig. 9). A damping term $K_p p_C$ is added based on low pass filtered low latency gyroscope measurements p_C, which measures rotations around the onboard camera X-axis. K_p is the so-called roll gyro gain.
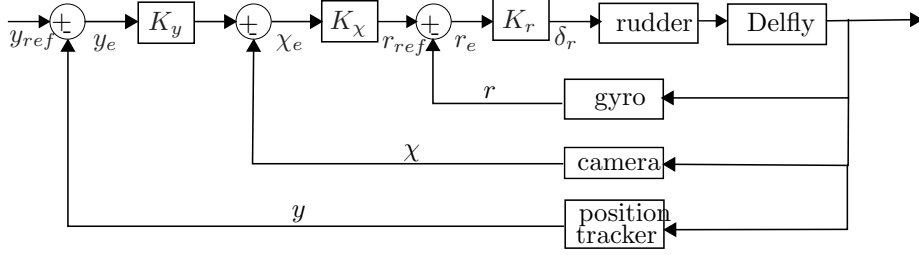
Figure 10: DelFly II lateral position controller.

During slow hovering flight the DelFly II flies almost nose up at very high pitch angles, while the rudder generated moments around the Z_D. To dampen Z_D oscillations a yaw damper is added constructed from the rates r_C and p_C aligned with the Z_C and X_C axes respectively (Fig. 7)

$$r_D = r_C \cos(17°) + p_C \sin(17°) \tag{10}$$

$$\tag{11}$$

The yaw damper is inserted as $K_r r_D$ where K_r is the yaw damper gain. To reduce the steady state error an integrator term $K_y^I \int (y - y_{ref})$ is added, where K_y^I is the integrator gain. The total controller for slow forward flight becomes after dropping out y_{ref} which is zero for the middle of the wind tunnel

$$\delta_r = K_\mu \mu + K_p p_C + K_r r_D + K_y^I \int y + K_k \tag{12}$$

where K_k is a value trim to be set manually when necessary.

4.2 Lateral Control of Forward Flight

When the DelFly is flying at higher velocities, the reference LED right in front of the DelFly is out of view, because the camera is looking almost downwards. The first part of the total controller shown in Eq. 12 is replaced by

$$\delta_r = K_\chi (y_e K_y - \chi) \tag{13}$$

including the lateral off-set $y_e = (y_{ref} - y)$. The total three loop control scheme is shown in Fig. 10.

Including an integrator term, setting the desired lateral offset y_{ref} and some rewriting the total controller becomes

$$\delta_r = K_y y + K_\chi \chi + K_r r + K_y^I \int y + K_k \tag{14}$$

10

4.3 Longitudinal Control of Slow Forward Flight

When flying at low speeds, the thrust vector of the flapping wing DelFly II is pointing almost straight up. It mostly controls the climb rate while the elevator influences the forward position. During forward flight however throttle most influences the forward speed and elevator the altitude. So at slow hovering flight for the vertical position z we have

$$\delta_{th} = f_{PID}(z - z_{ref}) \tag{15}$$

and the horizontal position x

$$\delta_e = f_{PID}(x - x_{ref}) \tag{16}$$

where δ_{th} and δ_e are resp. the thrust and elevator input, z and x the current horizontal and vertical position and z_{ref}, x_{ref} the reference position we want to achieve. During flight the battery will drain and the voltage significantly drops, as shown in Fig. 11. This is well handled by the integral term in the controller removing the need for feed forward compensations.
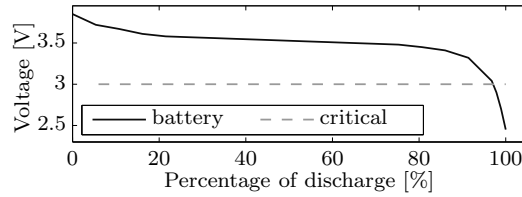

Figure 11: Typical Lithium-Polymer discharge curve of a single cell. DelFly II uses a single 180mAh cell as power source. As the voltage drops, the current is increased to keep the same power level.

For zero references the total control law for the throttle setting becomes

$$\delta_{th} = K_z z + K_z^I \int z + K_n \tag{17}$$

with K_z the proportional gain, K^I the integral gain and K_n the trim setting. Due to the very low wing loading high damping of DelFly II, the d-gain can be left out. For the elevator input

$$\delta_e = K_x x + K_x^I \int x + K_q q + K_m \tag{18}$$

is used where a pitch damper $K_q q$ is added and K_m is the trim setting.

11

4.4 Longitudinal Control of Forward flight

Unlike the slow hovering flight with rotorcraft-like characteristics, when the DelFly flies at higher velocities, the pitch angle decreases to about 30° for velocities around 2 m/s and upwards and the DelFly starts to behaves like a conventional fixed wing aircraft. The controls are configured to pitch from altitude error and throttle from speed error

$$\delta_e = f_{PID}(z - z_{ref}) \tag{19}$$
$$\delta_{th} = f_{PID}(x - x_{ref}) \tag{20}$$

The total control law for the throttle setting becomes then

$$\delta_{th} = K_x\ x + K_{v_x}v_x + K_x^I \int(x) + K_n \tag{21}$$

and for the elevator input

$$\delta_e = K_z\ z + K_{v_z}v_z + K_z^I \int(z) + K_q q + K_m \tag{22}$$

where $K_q\ q$ is the pitch damper, K_n and K_m the manual trim settings and the zero reference values x_{ref} and z_{ref} have been left out. The control laws very similar to the horizontal flight laws in Eq. 17 and Eq. 18, except that the axes on which controls surface act on are exchanged and position derivative terms are needed.

5 Station Keeping Experiments

A series of test and tuning flights were performed in the Open Jet Facility windtunnel of the Delft University of Technology. All gains were manually tuned in the various flight regimes. One must keep in mind that the hand built DelFly II weighs only 16 grams[8]. Imperfections, wear over time, undesired vibrations of the half a gram servos, resolution of all actuators and motor control, residual vortices in the wind tunnel as well as the lack of a full dynamics model for the development of the controller play important roles in the achievable performance.

A first series of tests tried to keep DelFly II as close as possible to the center of the tunnel. Results presented here concern slow hovering flight at $0.8m/s$. Fig. 12 show a test flight with relatively low value for the integrator gains. It shows how an untrimmed DelFly II rejects steady state errors.

A longer 14 minute flight in Fig. 13 shows the integrator nicely compensates for the dropping battery voltage (Fig. 11) by increasing the throttle over time.

Looking closer at the position signal, very low frequency oscillations are seen in the y and z direction, illustrated in Fig. 14. The resolution of throttle
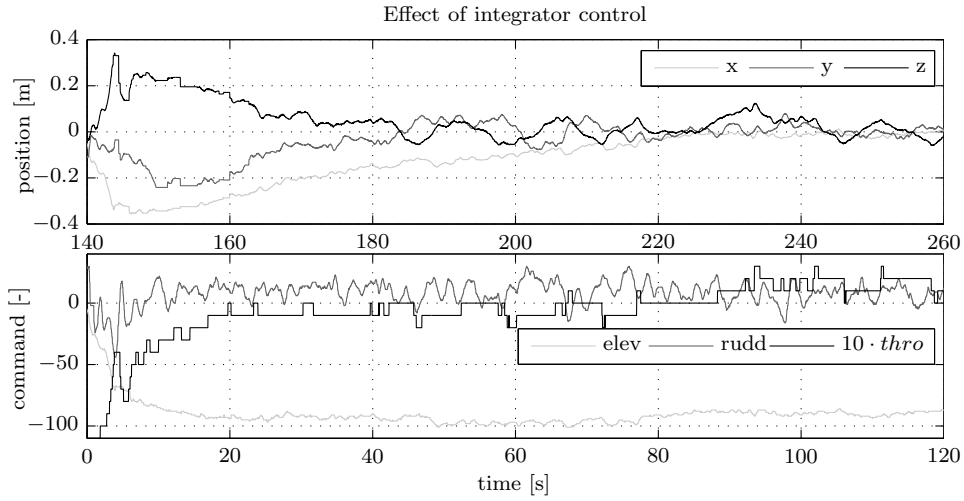
Figure 12: Initial test run with low integral gains while tuning the gains of the DelFly II without a full dynamic model.
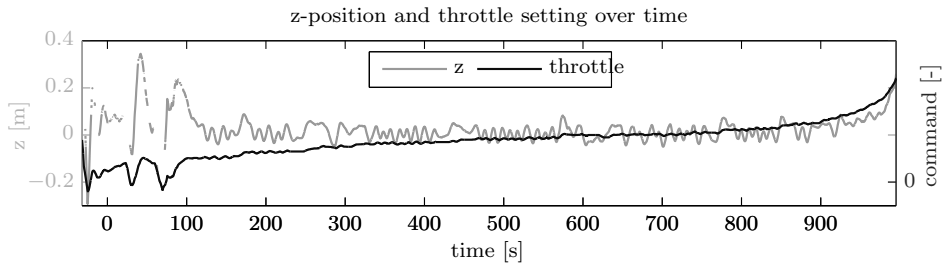

Figure 13: Required Power as function of Battery Voltage

control of DelFly II is only 170 discrete steps due to brushless motor controller constraints. This motor controller was specially developed to be able to face the highly non-constant load of the pushrods to the wings, flapping at about 13Hz. During a single flap cycle the motor must accelerate and decelerate with a 1 to 2 ratio. Additional trade-offs in the motor controller concerning efficiency make it hard to resolve this power resolution limitation.

Upon inspection it can be seen that the oscillations are driven by the throttle alternating between two values. The DelFly descents every time the throttle is reduced one unit, and ascends when the throttle is increased. When the battery voltage decreases over time as seen in Fig. 11, eventually the required power matches a settable power level and oscillations disappear. Table 1 shows the performance in this case and stands for the performance that could be obtained of finer throttle control were possible.

The manual tuning with the unknown dynamics of DelFly was done by performing many runs with different gains and searching for better RMS perfor-
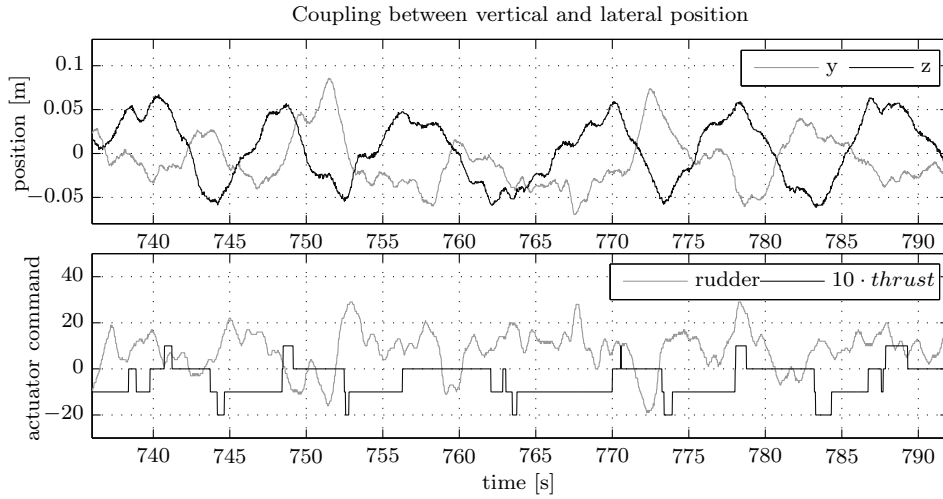
Figure 14: Close-up of a minute of autonomous flight. The throttle has been scaled 10× for clarity. It is alternating between one or two values. The y- and z-position are coupled: the DelFly moves up and right, or down and left, with a period of about 8 seconds.

direction	maximum deviation [cm]	RMS [cm]
x	1.6	0.82
y	4.3	1.8
z	1.5	0.95

Table 1: Maximum deviations from the windtunnel center and the RMS error values with correct power setting.

mance. Fig. 15 illustrates the effect of several yaw damping gains and Fig. 16 of several pitch damping gains on the station keeping performance of the DelFly II.
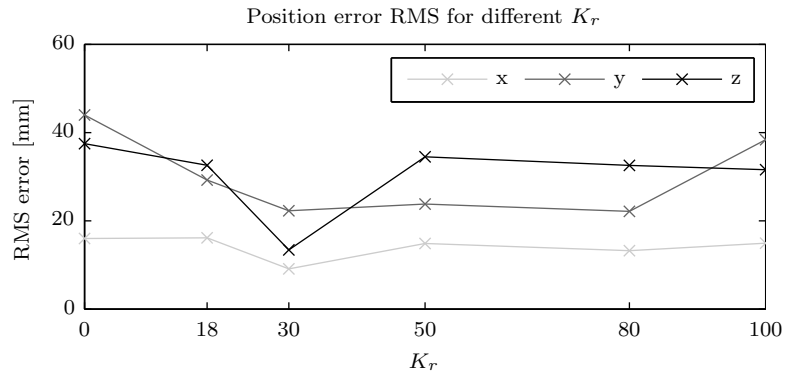
Position error RMS for different K_r

Figure 15: RMS error of the x,y and z position for different gain settings of the yaw damper. The sample duration was about 40 seconds for each setting.
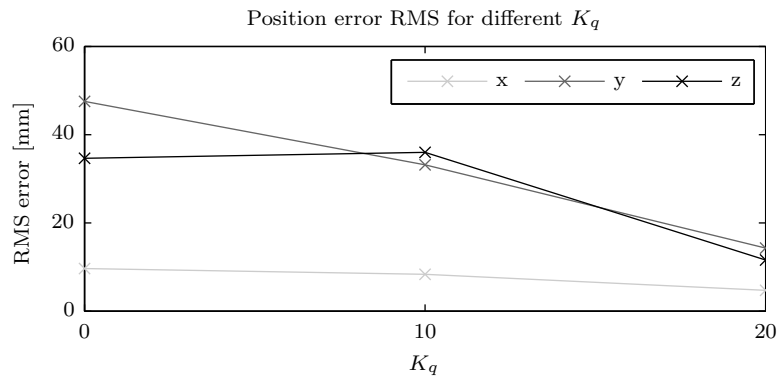
Position error RMS for different K_q

Figure 16: RMS error of the x,y and z position for different gain settings of the pitch damper.

6 Transient Behavior Experiments

In order to further analyze the stability and disturbance rejection of the system, and simultaneously obtain new information about the transient behavior of DelFly II, a series of step response tests were performed. These are depicted in Figures 17 to 20.
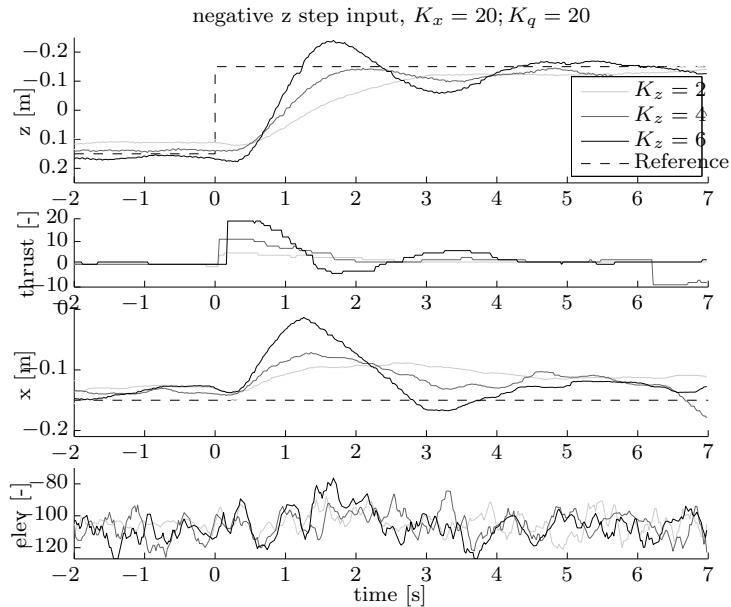
Figure 17: Step 30cm up. The throttle increase clearly results in a forward motion increase. For a gain of $K_z = 6$ the system shows under damped behavior, at K_2 over damped behavior.

7 Conclusions and Recommendations

A low-cost high performance control system is developed. The weight of the onboard part is less than two grams, while the sensors consists of only three WiiMote sensors, a few LED and a gyroscope chip. The total system station keeping performance was shown to be in the order of centimeters. The most important factors that limit the performance are the resolution of the power setting. Then the residual vorticity in the tunnel and unsteady periodic aerodynamics together with the 16 grams very low wing loading vehicle impose considerable perturbations to the control system, while manufacturing imperfections, wear over time and undesired vibrations of the miniature actuators also impact the performance. Nevertheless the achieved performance is still largely sufficient for many new research purposes, amongst which the analysis of the influence of fixing the fuselage in flapping wing research and more precise performance characteristics of DelFly II.

Aspects that need additional attention in further work are a lower latency data link to reduce delays and make them more constant than the Bluetooth modems. But most of all a increased throttle resolution, for instance using modulation techniques.
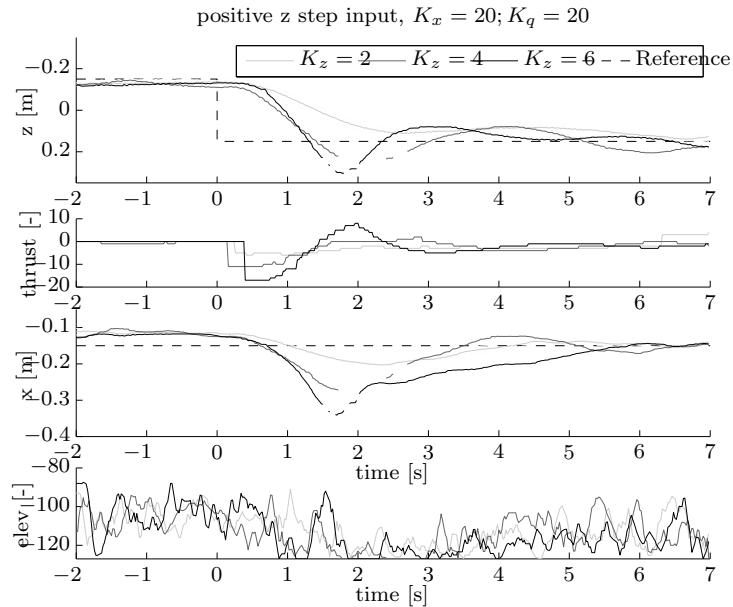
Figure 18: Step 30cm down. DelFly is drifted backwards due to the lower thrust setting which perturbs the horizontal equilibrium. Comparing with the step up, the same gain $K_z = 4$ shows overshoot instead of critical damping behavior, showing the high non-linearity in the behavior of DelFly II.

References

[1] Stanley Seunghoon Baek. *Autonomous Ornithopter Flight with Sensor-Based Behavior*. PhD thesis, University of California, Berkely, 2011.

[2] C. Van den Berg and C.P. Ellington. The three-dimensional leading-edge vortex of a hovering model hawkmoth. *Phil. Trans. R. Soc. Lond. B*, pages 329–340, 1997.

[3] W Biesel and W Nachtigall. Pigeon flight in a wind tunnel *. *Journal of Comparative Physiology B: Biochemical, Systemic, and Environmental Physiology*, pages 99–109, 1987.

[4] J.M. Birch, W.B. Dickson, and M.H. Dickinson. Force production and flow structure of the leading edge vortex on flapping wings at high and low reynolds numbers. *Journal of Experimental Biology*, 207(7):1063–1072, 2004.

[5] Richard J. Bomphrey, Nicholas J. Lawson, Graham K. Taylor, and Adrian L. R. Thomas. Application of digital particle image velocimetry to insect aerodynamics: measurement of the leading-edge vortex and near wake of a Hawkmoth. *Experiments in Fluids*, 40(4):546–554, January 2006.
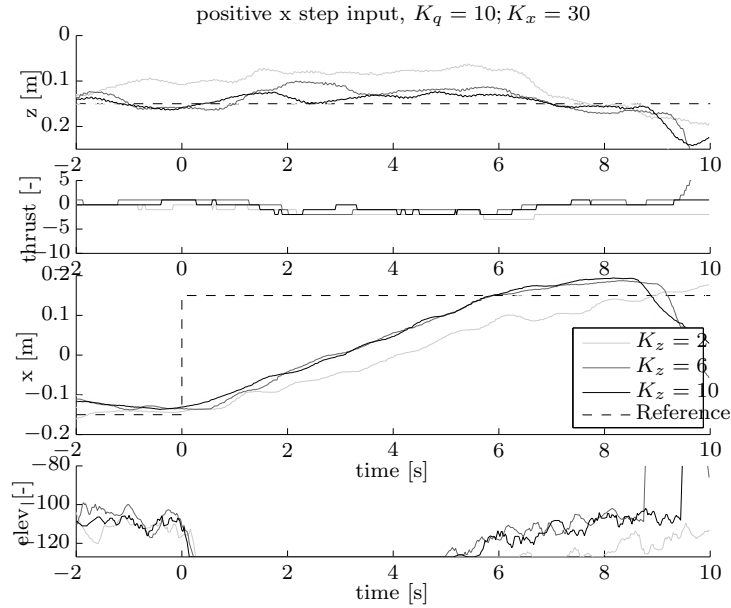
Figure 19: Horizontal 30cm step forward. The DelFly reacts very slowly due to saturation of the elevator. As slow hovering flight is on the negative side of the power curve, at higher forward speed less thrust is needed, which causes an upward perturbation.

[6] Nancy L Bradshaw and David Lentink. Aerodynamic and Structural Dynamic Identification of a flapping wing Micro Air Vehicle. *Aerospace Engineering*, (August):6248–6248, 2008.

[7] Kristien M E De Clercq, Roeland De Kat, Bart Remes, Bas W Van, and Hester Bijl. on DelFly II : Unsteady Lift Enhancement. *Measurement*, 1(4), 2009.

[8] G C H E De Croon, K M E De Clercq, R Ruijsink, and B Remes. Design, aerodynamics, and vision-based control of the DelFly. 1(2):71–98, 2009.

[9] Kristien M E De Clercq, Roeland De Kat, Bart Remes, Bas W Van Oudheusden, and Hester Bijl. Flow visualization and force measurements on a hovering flapping wing MAV Delfly II. *International Journal of Micro Air Vehicles*, 2009.

[10] MA Groen. PIV and force measurements on the flapping-wing MAV DelFly II. (December), 2010.

[11] Anders Hedenström, F. T. Muijres, R. Busse, L. C. Johansson, Y. Winter, and G. R. Spedding. High-speed stereo DPIV measurement of wakes of two bat species flying freely in a wind tunnel. *Experiments in Fluids*, 46(5):923–932, February 2009.
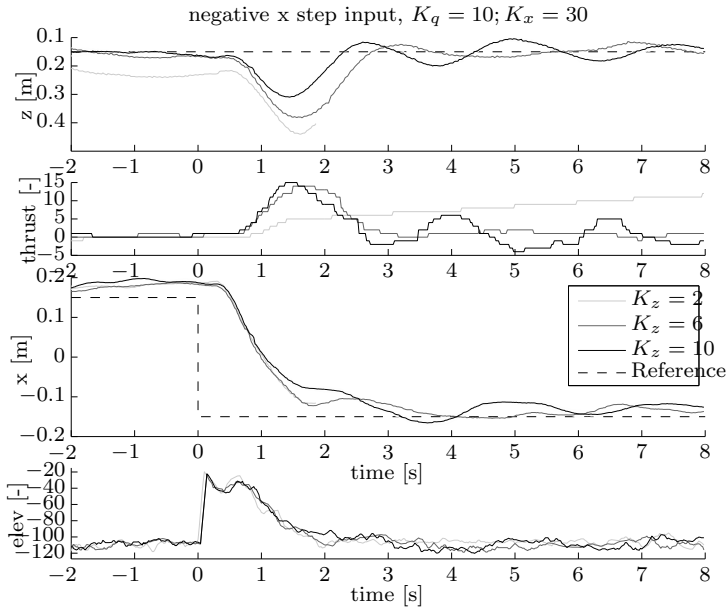
Figure 20: Horizontal 30cm back. DelFly reacts very quickly, drifting backward with the windtunnel flow. When flying at lower forward speed, extra thrust is needed which is visible as a descending perturbation for the altitude controller.

[12] D.-K. Kim, J.-H. Han, and K.-J. Kwon. Wind tunnel tests for a flapping wing model with a changeable camber using macro-fiber composite actuators. *Smart Materials and Structures*, 18(2), 2009.

[13] H. Liu and K. Kawachi. A numerical study of insect flight. *Journal of Computational Physics*, 146:124–156, 1998.

[14] G. F. Page. Multiple view geometry in computer vision, by richard hartley and andrew zisserman, cup, cambridge, uk, 2003, vi+560 pp., isbn 0-521-54051-8. *Robotica*, 23(2):271–271, March 2005.

[15] Darryll J. Pines and Felipe Bohorquez. Challenges facing future micro-air-vehicle development. *Journal of aircraft*, 43(2):290–305, 2006.

[16] C.E. Raffel, M., Willert and J. Wereley, S.T., Kompenhans. *Particle Image Velocimetry*. Springer, 2nd ed. edition, 2007.

[17] W. Thielicke, A.B. Kesel1, and E.J. Stamhuis. Reliable force predictions for a flapping-wing micro air vehicle: A "vortex-lift" approach. *International Journal of Micro Air Vehicles*, 3(4):201–216.

[18] Evan R Ulrich, Darryll J Pines, and J Sean Humbert. From falling to flying: the path to powered flight of a robotic samara nano air vehicle. *Bioinspiration & biomimetics*, 5(4):045009, December 2010.

[19] P.W. Willmot, C.P. Ellington, and A.L.R. Thomas. Flow visualization and unsteady aerodynamics in the flight of the hawkmoth, manduca sexta. *Phil. Trans.*, 1997.

[20] Jan Windte and K.-C. Pfingsten. On 2d motion parameters for flapping wing propulsion. In *European Micro Air Vehicle conference and competitions 2004*, pages 1–10, 2004.

[21] T. Yang, M. Wei, and H. Zhao. Numerical study of flexible flapping wing propulsion. *AIAA JOURNAL*, 48(12):2909–2915, 2010.